

Mathematical Representation of WECC Composite Load Model

Zixiao Ma, Zhaoyu Wang, Yishen Wang, Ruisheng Diao, and Di Shi

Abstract—Composite load model of Western Electricity Coordinating Council (WECC) is a newly developed load model that has drawn great interest from the industry. To analyze its dynamic characteristics with both mathematical and engineering rigors, a detailed mathematical model is needed. Although composite load model of WECC is available in commercial software as a module and its detailed block diagrams can be found in several public reports, there is no complete mathematical representation of the full model in literature. This paper addresses a challenging problem of deriving detailed mathematical representation of composite load model of WECC from its block diagrams. In particular, we have derived the mathematical representation of the new DER_A model. The developed mathematical model is verified using both MATLAB and PSS/E to show its effectiveness in representing composite load model of WECC. The derived mathematical representation serves as an important foundation for parameter identification, order reduction and other dynamic analysis.

Index Terms—Composite load model, dynamic load modeling, mathematical model, three-phase motor, DER_A model.

I. INTRODUCTION

LOAD modeling is essential to power system stability analysis, optimization, and controller design as shown in many researches [1]. Although the importance of load modeling is recognized by power system researchers and engineers [2], obtaining an accurate load model remains challenging. The difficulty is caused by the large number of diverse load components, time-varying compositions, and the lack of detailed load information and measurements. To this end, developing high-fidelity load models that approximate the real load characteristic while overcoming the above challenges is imperative.

Load modeling consists of developing model structures and identifying associated parameters. For a given load model structure, its parameter identification can be implemented

with component-based or measurement-based approaches. The component-based approach is based on the knowledge of detailed physical models with different load components and their compositions [3], [4]. However, the information is usually difficult to obtain, which motivates the research of measurement-based load modeling [5]-[10]. With the wider deployment of digital fault recorders, the measurement-based approaches become increasingly popular [6], [9], [11]-[13]. Measurement-based modeling uses the measured data to identify model parameters. The main advantage of this approach is that it collects the data directly from the power system and can be used for online modeling.

For the load model structure, there exist static and dynamic load models. For example, static load models include static constant impedance-current-power (ZIP) model and exponential model [4]. However, they cannot capture the dynamic behaviors of loads. Dynamic load models represent the real/reactive power as functions of both voltage and time such as induction motor (IM) model and exponential recovery load (ERL) model [14]-[16]. To consider both dynamic and static load characteristics, composite load models (CLMs) are proposed such as ZIP+IM load model, complex load model (CLOD), low-voltage (LV) load model and Western Electricity Coordinating Council (WECC) CLM. An aggregated five-machine dynamic equivalent electro-mechanical model of WECC power system using synchrophasor measurements is developed to bridge the gap aroused by the increasing penetration of renewable energy resources. These renewable energy resources will significantly change dynamic properties, inter-area oscillation characteristics and stability margins of WECC power systems in the near future [17]. However, this model is built from the perspective of the entire power system. After the blackout of the Western Systems Coordinating Council (WSCC) in 1996 [18], the ZIP+IM model is designed to capture the dynamic effects under highly stressed conditions in summer peaks. However, this interim model is ineffective in capturing delayed voltage recovery events from transmission faults [4], [19], [20]. By adding the electrical distance between the transmission system and the electrical end-uses as well as adding special components such as electronic load components and single-phase motors, a preliminary WECC CLM is proposed and implemented in major industry-level commercial simulation software packages [15]. With continuous updates and the incorporation of distributed energy resources (DERs), the newest WECC CLM, called CMPLDWG, is proposed as shown

Manuscript received: April 30, 2019; accepted: August 5, 2019. Date of Cross-Check: August 5, 2019. Date of online publication: XX XX, 2020.

This work was supported by the Power Systems Engineering Research Center (No. S-84G).

This article is distributed under the terms of the Creative Commons Attribution 4.0 International License (<http://creativecommons.org/licenses/by/4.0/>).

Z. Ma (corresponding author) and Z. Wang are with the Department of Electrical and Computer Engineering, Iowa State University, Ames, IA 50011, USA (e-mail: zma@iastate.edu; wzy@iastate.edu).

Y. Wang, R. Diao, and D. Shi are with GEIRI North America, San Jose, CA 95134, USA (e-mail: yishen.wang@geirina.net; ruisheng.diao@geirina.net; di.shi@geirina.net).

DOI: 10.35833/MPCE.2019.000296



in Fig. 1 [21]. The model includes an electrical representation of a distribution system with a substation transformer, shunt reactance, and a feeder equivalent. At the side of distribution system, it includes one static load model, one power electronic model, three three-phase motor models, one A/C single-phase motor and one DER. CMPLDWG uses PVD1 model to represent the DERs. However, PVD1 model consists of 5 modules, 121 parameters and 16 states, which is as complex as WECC CLM. Therefore, Electric Power Research Institute (EPRI) has developed a simpler yet more comprehensive model to replace PVD1 model, which is named as DER_A model [22].

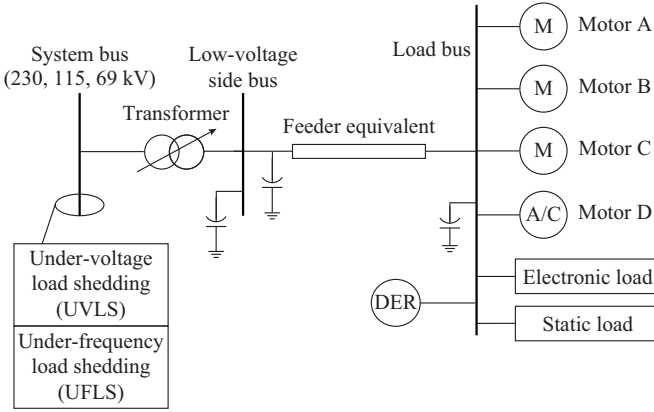


Fig. 1. Schematic diagram of CMPLDWG.

Although WECC CLM has been widely implemented in commercial software of power system, a comprehensive mathematical representation cannot be found in existing literature. Moreover, researchers cannot access the source codes of commercial software packages, making it hard to obtain the insights of the models implemented in the software. The detailed block diagrams of the model can be found in publicly available reports [22], [23]. However, deriving mathematical representation from these diagrams are challenging. In [24], one mathematical representation of three-phase motors has been provided, nevertheless, the DER_A model is missing. However, the mathematical model is essential for parameter identification, stability assessment, and dynamic order reduction. To this end, this paper derives a detailed and comprehensive mathematical representation of WECC CLM with DER_A model. Various simulations are conducted in both MATLAB and PSS/E to verify the effectiveness of the derived mathematical model.

The rest of the paper is organized as follows. Section II presents the detailed derivation of WECC CLM. Section III shows the simulation results and analysis. Section IV concludes the paper.

II. MATHEMATICAL MODELING OF INDIVIDUAL COMPONENTS

In this section, we will derive mathematical representations for individual components in WECC CLM, namely, three-phase motors, DER_A, single-phase motor, electronic and static loads.

A. Three-phase Motor Model

There are multiple types of three-phase induction motors that can describe the end-use loads [25]. In CMPLDWG, three different three-phase motors, A, B and C are used to represent different types of dynamic components. Motor A represents the three-phase induction motors with low-inertia driving constant torque loads, e.g., air conditioning compressor motors and positive displacement pumps. Motor B represents the three-phase induction motors with high-inertia driving variable torque loads such as commercial ventilation fans and air handling systems. Motor C represents the three-phase induction motors with low-inertia driving variable torque loads such as the common centrifugal pumps.

These three-phase motors share the same model structure. However, their model parameters are different. Therefore, a fifth-order induction motor model is adopted to represent three-phase motors in WECC CLM. Its block diagram is shown in Fig. 2, where $1/s$ denotes the integrator.

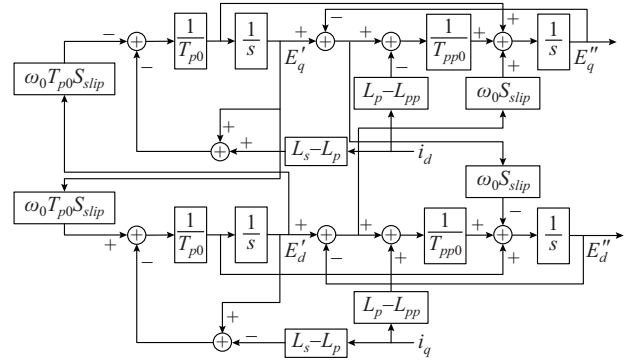


Fig. 2. Block diagram of three-phase motor.

From Fig. 2, we can obtain a fourth-order electrical model with respect to E'_q , E'_d , E''_q and E''_d . Combining with the mechanical model, we have the complete fifth-order model:

$$\dot{E}'_q = \frac{1}{T_{p0}} [-E'_q - i_d(L_s - L_p) - E'_d \omega_0 S_{slip} T_{p0}] \quad (1)$$

$$\dot{E}'_d = \frac{1}{T_{p0}} [-E'_d + i_q(L_s - L_p) + E'_q \omega_0 S_{slip} T_{p0}] \quad (2)$$

$$\dot{E}''_q = \frac{T_{p0} - T_{pp0}}{T_{p0} T_{pp0}} E'_q - \frac{T_{pp0}(L_s - L_p) + T_{p0}(L_p - L_{pp})}{T_{p0} T_{pp0}} i_d - \frac{1}{T_{pp0}} E''_q - \omega_0 S_{slip} E''_d \quad (3)$$

$$\dot{E}''_d = \frac{T_{p0} - T_{pp0}}{T_{p0} T_{pp0}} E'_d + \frac{T_{pp0}(L_s - L_p) + T_{p0}(L_p - L_{pp})}{T_{p0} T_{pp0}} i_q - \frac{1}{T_{pp0}} E''_d + \omega_0 S_{slip} E''_q \quad (4)$$

$$\dot{S}_{slip} = -\frac{pE''_d i_d + qE''_q i_q - TL}{2H} \quad (5)$$

The algebraic equations are:

$$TL = T_{m0} (Aw^2 + Bw + C + Dw^{E_{tra}}) \quad (6)$$

$$T_{m0} = pE''_{d0} i_{d0} + qE''_{q0} i_{q0} \quad (7)$$

$$w = 1 - S_{slip} \quad (8)$$

$$i_d = \frac{r_s}{r_s^2 + L_{pp}^2} (V_d + E_d'') + \frac{L_{pp}}{r_s^2 + L_{pp}^2} (V_q + E_q'') \quad (9)$$

$$i_q = \frac{r_s}{r_s^2 + L_{pp}^2} (V_q + E_q'') - \frac{L_{pp}}{r_s^2 + L_{pp}^2} (V_d + E_d'') \quad (10)$$

$$P = V_d i_d + V_q i_q \quad (11)$$

$$Q = V_d i_q - V_q i_d \quad (12)$$

where the five state variables are E_q' , E_d' , E_q'' , E_d'' , and S_{slip} ; L_s , r_s , L_p , and L_{pp} are the synchronous reactance, resistance, transient and subtransient reactances, respectively; T_{p0} and T_{pp0} are the transient and subtransient rotor time constants, respectively; ω_0 is the synchronous frequency; H is the inertia constant; i_d and i_q are terminal currents of dq -axes; p and q are constant coefficients which are predefined as -1 ; w is the motor speed; A , B , C , D are the speed coefficients of mechanical torque; E_{inq} is the torque damping coefficient; T_{m0} is the initial mechanical input torque; V_d and V_q are terminal voltages of dq -axes; and P and Q are the active and reactive power consumptions of the motor, respectively.

B. Single-phase Motor Model

Motor D in Fig. 1 represents the single-phase motor mod-

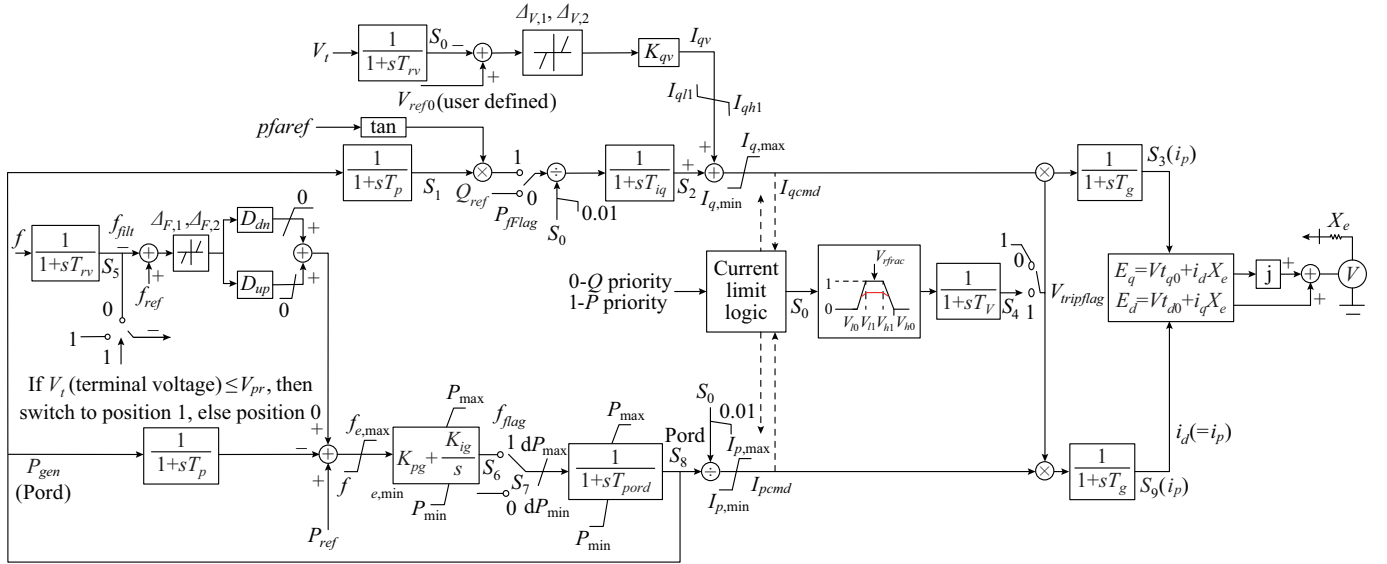


Fig. 3. Diagram of DER_A model.

1) Mathematical Model of S_0

Figure 4 shows the block diagram of first-order filter and we can obtain the following dynamic equation:

$$\dot{S}_0 = \frac{1}{T_{rv}} (V_t - S_0) \quad (13)$$

where T_{rv} is the transducer time constant for voltage measurement; V_t is the bus voltage; and S_0 is the filtered voltage V_{filtr} .

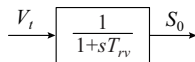


Fig. 4. Local block diagram of S_0 in DER_A model.

2) Mathematical Model of S_1

Figure 5 shows the block diagram of the first-order filter, whose input is the electrical power P_{gen} (S_8) generated at the terminals of DER_A model, and the output is the filtered power S_1 .

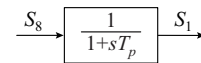


Fig. 5. Local block diagram of S_1 in DER_A model.

From Fig. 5, we can obtain the dynamic equation as:

$$\dot{S}_1 = \frac{1}{T_p} (S_8 - S_1) \quad (14)$$

el that captures the behaviors of single-phase air with reciprocating compressors. However, it is challenging to model the fault point on wave [26] and voltage ramping effects [25]. Moreover, the new motors A and C are mostly equipped with scroll compressors and/or power electronic drives, making their dynamic characteristics significantly different from the conventional motors. Therefore, WECC uses a performance-based model to represent single-phase motors. The main purpose of deriving the mathematical model is to establish the foundation for theoretical studies such as parameter identification and order reduction. Hence, it is unnecessary to derive the mathematical representation of the performance-based model.

C. DER_A Model

The DER_A is a newly developed model representing aggregate renewable energy resources. Compared to the previous PVD1 model which is relatively large and complex, the DER_A model has fewer states and parameters. There is no mathematical representation of the DER_A model in the existing literature till now. In this section, the detailed mathematical model is derived from Fig. 3 with respect to each state variable [21].

where T_p is the transducer time constant.

3) Mathematical Model of S_2

The local block diagram of S_2 is shown in Fig. 6 and we can obtain the following dynamic equation as:

$$\dot{S}_2 = \begin{cases} -\frac{S_2}{T_{iq}} + \frac{Q_{ref}}{T_{iq} \cdot sat_1(S_0)} & P_{fFlag} = 0 \\ -\frac{S_2}{T_{iq}} + \frac{S_1 \tan(pfaref)}{T_{iq} \cdot sat_1(S_0)} & P_{fFlag} = 1 \end{cases} \quad (15)$$

where Q_{ref} is determined based on the initial P output of DER_A model in software; $pfaref$ can be computed by $\arctan(Q_{gen0}/P_{gen0})$, Q_{gen0} and P_{gen0} are the active power and reactive power determined by the initial power flow solution, respectively; and T_{iq} is Q control time constant. The limiter in the diagram is described by a saturation function that can be defined as:

$$sat_1(x) = \begin{cases} x & x > 0.01 \\ 0.01 & x \leq 0.01 \end{cases} \quad (16)$$

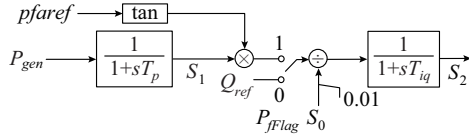


Fig. 6. Local block diagram of S_2 in DER_A model.

4) Mathematical Model of S_3

The local block diagram of the current of q -axis $S_3(i_q)$ is shown in Fig. 7.

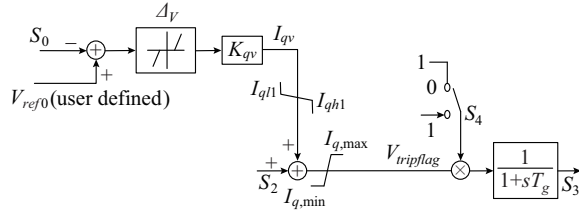


Fig. 7. Local block diagram of S_3 in DER_A model.

From Fig. 7, we can obtain the dynamic equation as:

$$\dot{S}_3 = \begin{cases} \frac{sat_2(S_2 + sat_3(g_{db,V}(V_{ref0} - S_0)K_{qv})) - S_3}{T_g} & V_{tripflag} = 0 \\ \frac{sat_2(S_2 + sat_3(g_{db,V}(V_{ref0} - S_0)K_{qv}))S_4 - S_3}{T_g} & V_{tripflag} = 1 \end{cases} \quad (17)$$

where V_{ref0} is the voltage reference of set-point; T_g is the current control time constant; and K_{qv} is the proportional voltage control gain. Voltage tripping is disabled when $V_{tripflag} = 0$, and it is enabled when $V_{tripflag} = 1$. The limiter functions and voltage dead band function are defined as:

$$sat_2(x) = \begin{cases} I_{q,max} & x \geq I_{q,max} \\ x & I_{q,min} < x < I_{q,max} \\ I_{q,min} & x \leq I_{q,min} \end{cases} \quad (18)$$

$$sat_3(x) = \begin{cases} I_{qh1} & x \geq I_{qh1} \\ x & I_{ql1} < x < I_{qh1} \\ I_{ql1} & x \leq I_{ql1} \end{cases} \quad (19)$$

$$g_{db,V}(x) = \begin{cases} x - \Delta_{V,1} & x > \Delta_{V,1} \\ 0 & \Delta_{V,2} \leq x \leq \Delta_{V,1} \\ x - \Delta_{V,2} & x < \Delta_{V,2} \end{cases} \quad (20)$$

where I_{ql1} and I_{qh1} are the minimum and maximum limits of reactive current injection, respectively; and $\Delta_{V,1}$ and $\Delta_{V,2}$ are the lower and upper voltage deadbands, respectively. The current limit is modeled as:

1) Q -priority: $I_{q,max} = I_{max}$, $I_{q,min} = -I_{max}$, where I_{max} is the maximum converter current.

2) P -priority: $I_{q,max} = \sqrt{I_{max}^2 - I_{pcmd}^2}$, $I_{q,min} = -I_{q,max}$, where I_{pcmd} is the active power command.

5) Mathematical Model of S_4

The local block diagram of S_4 is shown in Fig. 8. The first block is a function of voltage tripping logic. Denoting it by a piecewise function as (21), we can obtain the dynamic equation (22).

$$g_{vp}(S_0, V_{frac}) = \begin{cases} \frac{V_t - V_{l0}}{V_{l1} - V_{l0}} & V_{l0} \leq V_t \leq V_{min} \\ \frac{V_t - V_{l0}}{V_{l1} - V_{l0}} & V_{min} < V_t \leq V_{l1}, t \leq t_{lv1} \\ 1 & V_{l1} < V_t < V_{h1}, t \leq t_{lv1} \\ \frac{V_{h0} - V_t}{V_{h0} - V_{h1}} & V_{h1} \leq V_t \leq V_{h0}, t \leq t_{hv1} \\ V_{frac} \frac{V_t - V_{min}}{V_{l1} - V_{l0}} & V_{min} \leq V_t \leq V_{l1}, t \geq t_{lv1} \\ V_{frac} \frac{V_{l1} - V_{min}}{V_{l1} - V_{l0}} & V_{l1} < V_t < V_{h1}, t \geq t_{lv1} \\ V_{frac} \frac{V_{max} - V_t}{V_{h0} - V_{h1}} & V_{h1} \leq V_t \leq V_{max}, t \geq t_{hv1} \\ \frac{V_{h0} - V_t}{V_{h0} - V_{h1}} & V_{max} < V_t \leq V_{h0} \\ 0 & \text{otherwise} \end{cases} \quad (21)$$

$$\dot{S}_4 = \frac{1}{T_v} (g_{vp}(S_0, V_{frac}) - S_4) \quad (22)$$

where T_v is the time constant on the output of the voltage/frequency cut-off; V_{l0} and V_{l1} are the voltage break-points for low voltage cutout of inverters; V_{h0} and V_{h1} are the voltage break-points for high voltage cut-out of inverters; t_{lv1} is the timer for V_{l1} point; t_{hv1} is the timer for V_{h1} point; and V_{frac} is the fraction of device that recovers after voltage comes back to within $V_{l1} < V < V_{h1}$.

Note that V_{min} and V_{max} are determined by internal software which keeps tracking the minimum voltage of V_t during a simulation. Moreover, the frequency tripping logic is designed as follows: if the frequency goes below f_l for more than t_{fl} , then the entire model will trip; if the frequency goes above f_h for more than t_{fh} , then the entire model will trip.

6) Mathematical Model of S_5

Figure 9 shows the block diagram of first-order filter. From the diagram, we can obtain the dynamic equation as:

$$\dot{S}_5 = \frac{1}{T_{rf}} (f - S_5) \quad (23)$$

where T_{rf} is the transducer time constant for frequency measurement and $T_{rf} \geq 0.02$ s; f is the terminal frequency; and S_5 is the filtered frequency f_{filt} .

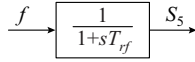


Fig. 9. Local block diagram of S_5 in DER_A model.

7) Mathematical Model of S_6

Figure 10 shows the diagram of proportional-integral (PI) controller with respect to S_6 . Defining the limiter and dead band functions as (19) - (30), we can obtain the following model of S_6 :

$$\begin{aligned} \dot{S}_6 = & K_{ig} sat_4 (P_{ref} - S_1 + sat_5 (D_{dn} g_{db,F} (f_{ref} - S_5)) + \\ & sat_6 (D_{up} g_{db,F} (f_{ref} - S_5))) + \frac{K_{pg}}{T_p} S_1 + G_{dn} (f - S_5) + G_{up} (f - S_5) - \frac{S_8}{T_p} \end{aligned} \quad (24)$$

$$sat_4(x) = \begin{cases} f_{e,max} & x \geq f_{e,max} \\ x & f_{e,min} < x < f_{e,max} \\ f_{e,min} & x \leq f_{e,min} \end{cases} \quad (25)$$

$$sat_5(x) = \begin{cases} x & x \leq 0 \\ 0 & x > 0 \end{cases} \quad (26)$$

$$sat_6(x) = \begin{cases} x & x > 0 \\ 0 & x \leq 0 \end{cases} \quad (27)$$

$$g_{db,F}(x) = \begin{cases} x - \Delta_{F,2} & x > \Delta_{F,2} \\ 0 & \Delta_{F,1} \leq x \leq \Delta_{F,2} \\ x - \Delta_{F,1} & x < \Delta_{F,1} \end{cases} \quad (28)$$

$$G_{dn}(x) = \begin{cases} -\frac{K_{pg} D_{dn}}{T_{rf}} x & x < \Delta_{F,1} \text{ or } x > \Delta_{F,2}, \frac{D_{dn}}{T_{rf}} x \geq 0 \\ 0 & \text{otherwise} \end{cases} \quad (29)$$

$$G_{up}(x) = \begin{cases} -\frac{K_{pg} D_{up}}{T_{rf}} x & x < \Delta_{F,1} \text{ or } x > \Delta_{F,2}, \frac{D_{up}}{T_{rf}} x < 0 \\ 0 & \text{otherwise} \end{cases} \quad (30)$$

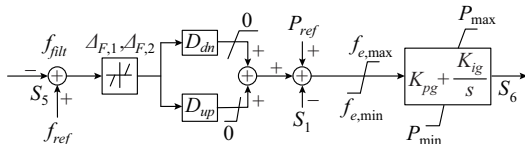


Fig. 10. Local block diagram of S_6 in DER_A model.

8) Mathematical Model of S_7

The local block diagram of S_7 is shown in Fig. 11. From the diagram, we can obtain the following dynamic equation:

$$\dot{S}_7 = \begin{cases} 0 & f_{flag} = 0 \\ sat_8 (sat_7 (S_6)) & f_{flag} = 1 \end{cases} \quad (31)$$

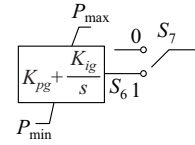


Fig. 11. Local block diagram of S_7 in DER_A model.

When $f_{flag} = 0$, frequency control is disabled and when $f_{flag} = 1$, frequency control is enabled. The limiter function is:

$$sat_7(x) = \begin{cases} P_{max} & x \geq P_{max} \\ x & P_{min} < x < P_{max} \\ P_{min} & x \leq P_{min} \end{cases} \quad (32)$$

$$sat_8(x) = \begin{cases} dP_{max} & x \geq dP_{max} \\ x & dP_{min} < x < dP_{max} \\ dP_{min} & x \leq dP_{min} \end{cases} \quad (33)$$

where P_{min} and P_{max} are the minimum and maximum power, respectively; and dP_{min} and dP_{max} are the lower and upper power ramp rates, respectively.

9) Mathematical Model of S_8

The local block diagram of S_8 is shown in Fig. 12. From the diagram, we can obtain the following dynamic equation:

$$\dot{S}_8 = \frac{1}{T_{pord}} (S_7 - S_8) \quad (34)$$

where T_{pord} is the power order time constant; and S_8 is the power order (Pord).

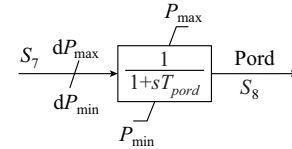


Fig. 12. Local block diagram of S_8 in DER_A model.

10) Mathematical Model of S_9

The local block diagram of the current of d -axis S_9 (i_p) is shown in Fig. 13, from which, we can obtain:

$$\dot{S}_9 = \begin{cases} \frac{1}{T_g} \left(sat_9 \left(\frac{sat_7 (S_8)}{sat_1 (S_0)} \right) S_4 - S_9 \right) & V_{tripflag} = 1 \\ \frac{1}{T_g} \left(sat_9 \left(\frac{sat_7 (S_8)}{sat_1 (S_0)} \right) - S_9 \right) & V_{tripflag} = 0 \end{cases} \quad (35)$$

When $V_{tripflag} = 0$, the voltage tripping is disabled, otherwise, it is enabled. The limiter functions are defined as (16), (32) and (36).

$$sat_9(x) = \begin{cases} I_{p,max} & x \geq I_{p,max} \\ x & I_{p,min} < x < I_{p,max} \\ I_{p,min} & x \leq I_{p,min} \end{cases} \quad (36)$$

The current limit is modeled as:

1) Q -priority: $I_{p,max} = \sqrt{I_{max}^2 - I_{qcmd}^2}$, where I_{qcmd} is the reactive power command. If the unit is a storage device, $I_{p,min} = -I_{p,max}$; if the unit is a generator, $I_{p,min} = 0$.

2) P -priority: $I_{p,max} = I_{max}$. If the unit is a storage device, $I_{p,min} = -I_{p,max}$; if the unit is a generator, $I_{p,min} = 0$.

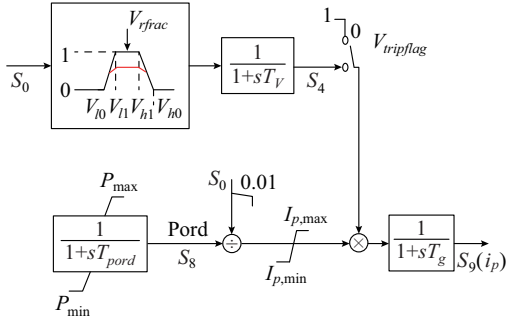


Fig. 13. Local block diagram of S_9 in DER_A model.

D. Static Load Model

In CMPLDWG, the classic ZIP model is adopted to represent the static load [24]. The ZIP model consists of constant impedance (Z), constant current (I) and constant power (P) components. It is usually used to represent the relationship between output power and input voltage. The mathematical representation is given as:

$$P_{ZIP} = P_0 \left[a_p \left(\frac{V}{V_0} \right)^2 + b_p \frac{V}{V_0} + c_p \right] \quad (37)$$

$$Q_{ZIP} = Q_0 \left[a_q \left(\frac{V}{V_0} \right)^2 + b_q \frac{V}{V_0} + c_q \right] \quad (38)$$

where P_{ZIP} and Q_{ZIP} are the active power and reactive power at the bus of interest, respectively; V_0 is the nominal voltage; P_0 and Q_0 are the base active and reactive power, respectively; V is the voltage magnitude; a_p , b_p , c_p are the parameters for active power of the ZIP load, and they satisfy $a_p + b_p + c_p = 1$; a_q , b_q , c_q are the parameters for the reactive power of the ZIP load, and they satisfy $a_q + b_q + c_q = 1$; $a_p P_0 (V/V_0)^2$ in (37) represents the active power of the constant impedance load; $P_0 a_p / V_0^2$ is the constant conductance; $b_p P_0 (V/V_0)$ represents the active power of the constant current load; $P_0 b_p / V_0$ is the constant current; and $c_p P_0$ represents the constant power load.

E. Model of Electronic Load

The electronic load defined in CMPLDWG is similar to that defined in the software PowerWorld [27]. The mathematical representation is:

$$P_{E,t} = c_t P_{E,0} \quad (39)$$

$$Q_{E,t} = c_t Q_{E,0} \quad (40)$$

where $P_{E,t}$ and $Q_{E,t}$ are the active and reactive power of the electronic load at time t , respectively; c_t is a coefficient with respect to the bus voltage, and is defined in Table I [21]; and $P_{E,0}$ and $Q_{E,0}$ are the base active and reactive power, respectively. In Table I, V_{d1} and V_{d2} are two threshold values, and α is a fraction of the electronic load that recovers from low voltage trip. If α is larger than zero, it will be reconnected linearly as the voltage recovers. $V_{\min,t}$ is a value tracking the lowest voltage but not below V_{d2} , and it is a known value at each sample. Its value can be expressed as:

$$V_{\min,t} = \max \left\{ V_{d2}, \min \left\{ V_t, V_{\min,t-1} \right\} \right\} \quad (41)$$

TABLE I
COEFFICIENT OF ELECTRONIC LOAD

Value of c_t	Condition	Mode
0	$V_t < V_{d2}$	1
$\frac{V_t - V_{d2}}{V_{d1} - V_{d2}}$	$V_{d2} \leq V_t < V_{d1}, V_t \leq V_{\min,t}$	2
$\frac{V_{\min,t} - V_{d2} + \alpha(V_t - V_{\min,t})}{V_{d1} - V_{d2}}$	$V_{d2} \leq V_t < V_{d1}, V_t > V_{\min,t}$	3
1	$V_t \geq V_{d1}, V_{\min,t} \geq V_{d1}$	4
$\frac{V_{\min,t} - V_{d2} + \alpha(V_{d1} - V_{\min,t})}{V_{d1} - V_{d2}}$	$V_t \geq V_{d1}, V_{\min,t} < V_{d1}$	5

The modes depend on the terminal voltage following rules as below:

- 1) If the terminal voltage V_t is higher than the threshold value V_{d1} , the active power and reactive power of the electronic load are constant P and Q .
- 2) If the terminal voltage V_t is lower than the threshold value V_{d2} , the active power and reactive power of the electronic load are constant P and Q .
- 3) If the voltage V_t is between two threshold values V_{d1} and V_{d2} ($V_{d1} > V_{d2}$), the active power and reactive power of the electronic load are linearly reduced to zero.

III. MODEL VALIDATION VIA SIMULATION

In this section, the mathematical model derived in this paper is verified through simulation. The mathematical models of three-phase motor and DER_A are tested on MATLAB and PSS/E simultaneously. We compare the performance of the derived mathematical representation with WECC model embedded in PSS/E to show the accuracy of the derived one.

A. Validation of Three-phase Motors

To verify the proposed model of three-phase motor, we simulate the mathematical model in MATLAB and compare it with CMLDBLU2 load model provided by PSS/E. Since only the mathematical model of three-phase motor to be validated, the parameters other than three-phase motor in CMLDBLU2 are set to be zero. Moreover, the same bus voltage inputs are given to both models. Consequently, we can compare the output power of the proposed mathematical representation of three-phase motor with that in PSS/E. Refer to [21], the bus voltage input is generated by (42). The parameters are set in Table II [28].

$$V(t) = \begin{cases} a & 1 \leq t < 1 + b/60 \\ \frac{(1-d)(t-c-1)}{b/60-c} + 1 & 1 + b/60 \leq t \leq 1 + c \\ 1 & \text{otherwise} \end{cases} \quad (42)$$

where a is the voltage sag level; b is the sag duration; c is the ramp recovery time; and d is the ramp recovery starting level.

Figure 14 shows the bus voltage input of three-phase motor. Figures 15-17 show the dynamic power responses of mo-

tors A, B and C, respectively. The mean square errors (MSEs) between the proposed mathematical model and CMLDBLU2 model are shown in Table III. The small errors show the accuracy of the proposed mathematical model of three-phase motor.

TABLE II
PARAMETERS OF THREE-PHASE MOTOR MODEL

Parameter of motor A	Value	Parameter of motor B	Value	Parameter of motor C	Value
$r_{s,A}$	0.04 p.u.	$r_{s,B}$	0.03 p.u.	$r_{s,C}$	0.03 p.u.
$L_{s,A}$	1.8 p.u.	$L_{s,B}$	1.8 p.u.	$L_{s,C}$	1.8 p.u.
$L_{p,A}$	0.1 p.u.	$L_{p,B}$	0.16 p.u.	$L_{p,C}$	0.16 p.u.
$L_{pp,A}$	0.083 p.u.	$L_{pp,B}$	0.12 p.u.	$L_{pp,C}$	0.12 p.u.
$T_{po,A}$	0.092 s	$T_{po,B}$	0.1 s	$T_{po,C}$	0.1 s
$T_{ppo,A}$	0.002 s	$T_{ppo,B}$	0.0026 s	$T_{ppo,C}$	0.0026 s
H_A	0.05 s	H_B	1 s	H_C	0.1 s
A_A	0	A_B	0	A_C	0
B_A	0	B_B	0	B_C	0
C_A	0	C_B	0	C_C	0
D_A	1	D_B	1	D_C	1
$E_{irq,A}$	0	$E_{irq,B}$	2	$E_{irq,C}$	2
p_A	-1	p_B	-1	p_C	-1
q_A	-1	q_B	-1	q_C	-1
$\omega_{0,A}$	120π rad/s	$\omega_{0,B}$	120π rad/s	$\omega_{0,C}$	120π rad/s

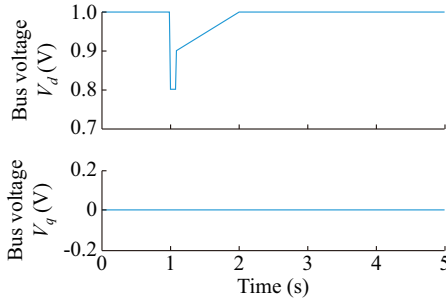


Fig. 14. Bus voltages of mathematical and PSS/E model of three-phase motor.

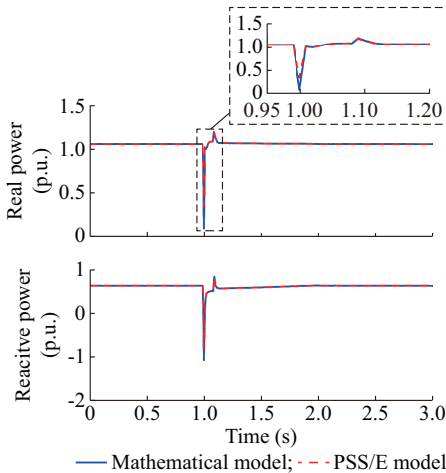


Fig. 15. Real and reactive power of mathematical and PSS/E models of three-phase motor A.

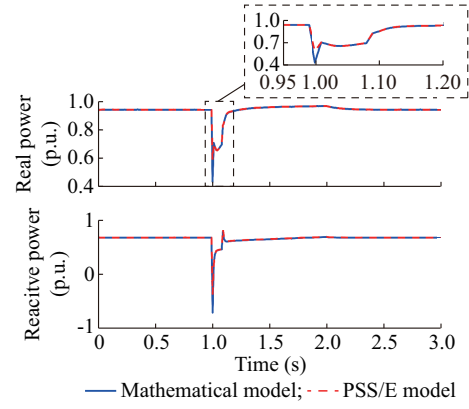


Fig. 16. Real and reactive power of mathematical and PSS/E models of three-phase motor B.

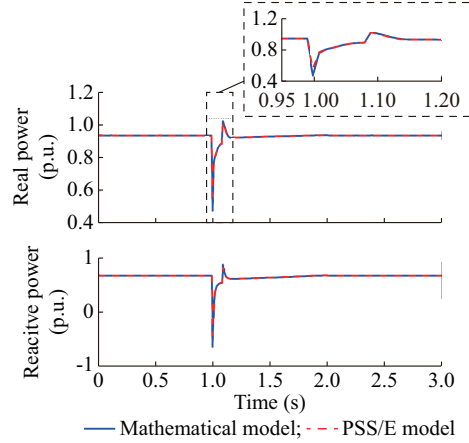


Fig. 17. Real and reactive power of mathematical and PSS/E models of three-phase motor C.

TABLE III
MSEs BETWEEN MATHEMATICAL MODEL AND CMLDBLU2 MODEL OF THREE-PHASE MOTOR

Power	MSE		
	Motor A	Motor B	Motor C
Real power	3.1109×10^{-7}	1.0291×10^{-5}	1.0263×10^{-5}
Reactive power	3.1325×10^{-5}	8.4974×10^{-5}	4.9115×10^{-5}

B. Validation of DER_A Model

Similar to the verification process of three-phase motor, we simulate the mathematical model of DER_A in MATLAB and adopt DERAU1 provided by PSS/E at the same time. Moreover, the same bus voltage and frequency inputs are given to both models. Consequently, we can compare the output power of the proposed mathematical representation of DER_A model with that in PSS/E. The voltage input is the same as (42). The frequency input is set to be 60 Hz. The base voltage is 12.47 kV. The base capacity is 15.0 MVA. The parameters are set as shown in Table IV [21], where $typeflag = 1$ represents the applied unit is a storage device.

Figure 18 shows the filtered bus voltage and frequency inputs of DER_A. Figure 19 shows the dynamic power responses of DER_A. The MSEs of real and reactive power are 1.1053×10^{-4} and 7.3079×10^{-5} , respectively. The small

error shows the accuracy of the proposed mathematical model of DER_A.

TABLE IV
PARAMETER SETTING OF DER_A MODEL

Parameter	Value	Parameter	Value
T_{rv}	0.02 s	T_p	0.02 s
T_{iq}	0.02 s	V_{ref0}	0
K_{qv}	5 p.u./p.u.	T_g	0.02 s
P_{fflag}	1	I_{max}	1.2 p.u.
$\Delta_{V,1}$	-99 p.u.	$\Delta_{V,2}$	99 p.u.
T_v	0.02 s	V_{f0}	0.44 p.u.
V_{f1}	0.49 p.u.	V_{h0}	1.2 p.u.
V_{h1}	1.15 p.u.	t_{v10}	0.16 s
t_{v1}	0.16 s	t_{v10}	0.16 s
t_{vh1}	0.16 s	V_{rfrac}	0.7
T_{rf}	0.02 s	K_{pg}	0.1 p.u.
K_{ig}	10 p.u.	D_{dn}	20
D_{up}	0	$f_{e,max}$	99 p.u.
$f_{e,min}$	-99 p.u.	$\Delta_{F,1}$	-0.0006
$\Delta_{F,2}$	0.0006	f_{flag}	0
P_{min}	0	P_{max}	1.1 p.u.
T_{pord}	0.02 s	dP_{min}	-0.5 p.u./s
dP_{max}	0.5 p.u./s	$V_{tripflag}$	1
I_{q1}	-1 p.u.	I_{qh1}	1 p.u.
X_e	0.25 p.u.	$F_{tripflag}$	1
PQ_{flag}	0	$typeflag$	1
V_{pr}	0.8 p.u.	a	0.8 p.u.
b	5	c	1 s
d	0.9 p.u.		

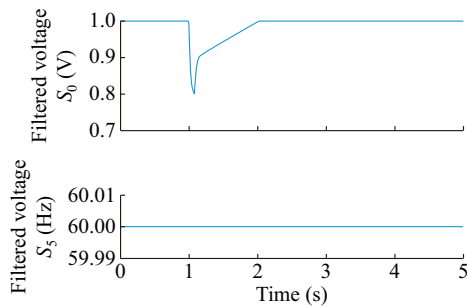


Fig. 18. Bus voltages and frequency of mathematical and PSS/E models of DER_A.

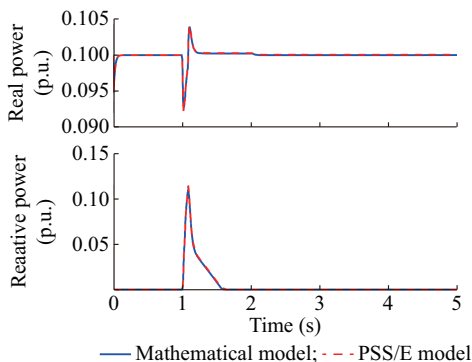


Fig. 19. Real and reactive power of mathematical and PSS/E models of DER_A.

IV. CONCLUSION

WECC CLM is important for power system monitoring, control and planning such as stability margin assessment, contingency analysis, impact assessment of renewable energy, and emergency load control. This paper develops the detailed mathematical model of three-phase motor and DER_A in WECC CLM. Several simulations are conducted in matlab and PSS/E. The comparison analysis shows the accuracy of the proposed mathematical representation. This detailed representation is useful for theoretical studies such as stability analysis, parameter identification, and order reduction.

REFERENCES

- [1] C. W. Taylor, N. Balu, and D. Maratukulam, *Power System Voltage Stability*. New York: McGraw-Hill, 1994.
- [2] P. Kundur, N. J. Balu, and M. G. Lauby, *Power System Stability and Control*. New York: McGraw-hill, 1994.
- [3] K. E. Wong, M. E. Haque, and M. Davies, "Component-based dynamic load modeling of a paper mill," in *Proceedings of 22nd Australasian Universities Power Engineering Conference (AUPEC)*, Bali, Indonesia, Sept. 2012, pp. 1-6.
- [4] D. Kosterev, A. Meklin, J. Undrill *et al.*, "Load modeling in power system studies: WECC progress update," in *Proceedings of IEEE PES General Meeting - Conversion and Delivery of Electrical Energy in the 21st Century*, Pittsburgh, USA, Jul. 2008, pp. 1-8.
- [5] S. H. Lee, S. E. Son, S. M. Lee *et al.*, "Kalman-filter based static load modeling of real power system using K-EMS data," *Journal of Electrical Engineering Technology*, vol. 7, no. 3, pp. 304-311, Jun. 2012.
- [6] J. Ma, D. Han, R. He *et al.*, "Reducing identified parameters of measurement-based composite load model," *IEEE Transactions on Power Systems*, vol. 23, no. 1, pp. 76-83, Feb. 2008.
- [7] I. F. Visconti, D. A. Lima, J. M. C. Costa *et al.*, "Measurement-based load modeling using transfer functions for dynamic simulations," *IEEE Transactions on Power Systems*, vol. 29, no. 1, pp. 111-120, Jan. 2014.
- [8] D. Han, J. Ma, R. He *et al.*, "A real application of measurement-based load modeling in large-scale power grids and its validation," *IEEE Transactions on Power Systems*, vol. 24, no. 4, pp. 1756-1764, Nov. 2009.
- [9] B. Choi and H. Chiang, "Multiple solutions and plateau phenomenon in measurement-based load model development: issues and suggestions," *IEEE Transactions on Power Systems*, vol. 24, no. 2, pp. 824-831, May 2009.
- [10] F. Hu, K. Sun, A. D. Rosso *et al.*, "Measurement-based real-time voltage stability monitoring for load areas," *IEEE Transactions on Power Systems*, vol. 31, no. 4, pp. 2787-2798, Jul. 2016.
- [11] S. Son, S. H. Lee, D. Choi *et al.*, "Improvement of composite load modeling based on parameter sensitivity and dependency analyses," *IEEE Transactions on Power Systems*, vol. 29, no. 1, pp. 242-250, Jan. 2014.
- [12] J. Kim, K. An, J. Ma *et al.*, "Fast and reliable estimation of composite load model parameters using analytical similarity of parameter sensitivity," *IEEE Transactions on Power Systems*, vol. 31, no. 1, pp. 663-671, Jan. 2016.
- [13] S. Guo and T. J. Overbye, "Parameter estimation of a complex load model using phasor measurements," in *Proceedings of IEEE Power and Energy Conference at Illinois*, Champaign, USA, Feb. 2012, pp. 1-6.
- [14] I. A. Hiskens, "Nonlinear dynamic model evaluation from disturbance measurements," *IEEE Transactions on Power Systems*, vol. 16, no. 4, pp. 702-710, Nov. 2001.
- [15] A. Arif, Z. Wang, J. Wang *et al.*, "Load modeling a review," *IEEE Transactions on Smart Grid*, vol. 9, no. 6, pp. 5986-5999, Nov. 2018.
- [16] Q. Huang, R. Huang, B. J. Palmer *et al.*, "A generic modeling and development approach for WECC composite load model," *Electric Power Systems Research*, vol. 172, pp. 1-10, Jul. 2019.
- [17] G. Chavan, M. Weiss, A. Chakraborty *et al.*, "Identification and predictive analysis of a multi-area WECC power system model using synchrophasors," *IEEE Transactions on Smart Grid*, vol. 8, no. 4, pp. 1977-1986, Jul. 2017.
- [18] D. N. Kosterev, C. W. Taylor, and W. A. Mittelstadt, "Model validation for the August 10, 1996 WSCC system outage," *IEEE Transac-*

- tions on *Power Systems*, vol. 14, no. 3, pp. 967-979, Aug. 1999.
- [19] B. R. Williams, W. R. Schmus, and D. C. Dawson, "Transmission voltage recovery delayed by stalled air conditioner compressors," *IEEE Transactions on Power Systems*, vol. 7, no. 3, pp. 1173-1181, Aug. 1992.
- [20] J. W. Shaffer, "Air conditioner response to transmission faults," *IEEE Transactions on Power Systems*, vol. 12, no. 2, pp. 614-621, May 1997.
- [21] WECC, "WECC dynamic composite load model (CMLPDW) specifications," Technical Report, Jan. 2015.
- [22] Electrical Power Research Institute, "The new aggregated distributed energy resources (DER A) model for transmission planning studies: 2019 update," Technical Report, 2019.
- [23] S. Wang, "Introduction to WECC modeling and validation work group," Technical Report, May 2018.
- [24] Q. Huang, R. Huang, B. J. Palmer *et al.*, "A reference implementation of WECC composite load model in MATLAB and GridPACK," arXiv: 1708.00939.
- [25] North American Reliability Cooperation, "Technical reference document: dynamic load modeling," Technical Report, Dec. 2016.
- [26] Q. Huang and V. Vittal, "Application of electromagnetic transient-transient stability hybrid simulation to FIDVR study," *IEEE Transactions on Power Systems*, vol. 31, no. 4, pp. 2634-2646, Jul. 2016.
- [27] C. Wang, Z. Wang, J. Wang *et al.*, "SVM-based parameter identification for composite ZIP and electronic load modeling," *IEEE Transactions on Power Systems*, vol. 34, no. 1, pp. 182-193, Jan. 2019.
- [28] K. Zhang, H. Zhu, and S. Guo, "Dependency analysis and improved parameter estimation for dynamic composite load modeling," *IEEE Transactions on Power Systems*, vol. 32, no. 4, pp. 3287-3297, Jul. 2017.

Zixiao Ma received his B.S. degree in automation and M.S. degree in control theory and control engineering from Northeastern University, Shenyang, China, in 2014 and 2017, respectively. He is now a Ph.D. student in the Department of Electrical and Computer Engineering at the Iowa State University, Ames, USA. His research interests include power system load modeling, microgrids, nonlinear control and model order reduction.

Zhaoyu Wang received the B.S. and M.S. degrees in electrical engineering from Shanghai Jiaotong University, Shanghai, China, in 2009 and 2012, respectively, and the M.S. and Ph.D. degrees in electrical and computer engineering from Georgia Institute of Technology, Atlanta, USA, in 2012 and 2015, respectively. He is now the Harpole-Pentair Assistant Professor with

Iowa State University, Ames, USA. He was a Research Aid at Argonne National Laboratory, Chicago, USA, in 2013 and an Electrical Engineer Intern at Corning Inc. in 2014. He is the Principal Investigator for a multitude of projects focused on these topics and funded by the National Science Foundation, the Department of Energy, National Laboratories, PSERC, and Iowa Energy Center. He received the IEEE PES General Meeting Best Paper Award in 2017 and the IEEE Industrial Application Society Prize Paper Award in 2016. He is the Secretary of IEEE Power and Energy Society Award Subcommittee. He is an editor of IEEE Transactions on Power Systems, IEEE Transactions on Smart Grid and IEEE PES Letters, and an associate editor of IET Smart Grid. His research interests include power distribution systems, microgrids, renewable integration, power system resilience, and data-driven system modeling.

Yishen Wang received the B.S. degree in electrical engineering from Tsinghua University, Beijing, China, in 2011, the M.S. and the Ph.D. degrees in electrical engineering from the University of Washington, Seattle, USA, in 2013 and 2017, respectively. He is currently a Power System Research Engineer with Global Energy Interconnection Research Institute North America, San Jose, USA. His research interests include power system economics and operation, energy storage, microgrids, load modeling and phasor measurement unit data analytics.

Ruisheng Diao received his Ph.D. degree in electrical engineering from Arizona State University, Tempe, USA, in 2009. Serving as a project manager, PI/co-PI and key technical contributor, he has been managing and supporting a portfolio of research projects in the area of power system modeling, dynamic simulation, online security assessment and control, dynamic state estimation, integration of renewable energy, and HPC implementation in power grid studies. He is now with Global Energy Interconnection Research Institute North America as deputy department head of phasor measurement unit & System Analytics, in charge of several R&D projects on power grid high-fidelity simulation tools and developing new artificial intelligence methods for grid operations.

Di Shi received the B. S. degree in electrical engineering from Xi'an Jiaotong University, Xi'an, China, in 2007, and M.S. and Ph.D. degrees in electrical engineering from Arizona State University, Tempe, USA, in 2009 and 2012, respectively. He currently leads the phasor measurement unit & System Analytics Group at Global Energy Interconnection Research Institute North America, San Jose, USA. He is an Editor of IEEE Transactions on Smart Grid. His research interests include wide area measurement system (WAMS), energy storage systems, and renewable integration.